



Cracking Processes and Coalescence Modes in Rock-Like Specimens with Two Parallel Pre-existing Cracks

Cheng Zhao¹ · Yi meng Zhou¹ · Chun feng Zhao¹ · Chong Bao¹

Received: 8 July 2017 / Accepted: 1 June 2018 / Published online: 8 June 2018
© Springer-Verlag GmbH Austria, part of Springer Nature 2018

Abstract

The cracks in a rock tend to initiate, propagate, and coalesce under loading. Based on the digital image correlation (DIC) method, uniaxial compression tests are carried out on rock-like specimens with various arrangements of two parallel cracks. The full-field strain and failure features of the rock-like materials are observed and analysis by a self-developed code. Two process zones are defined according to the differences between the shear strain field and the tensile strain field: a shear process zone and a tensile process zone. The following results are obtained in this study. (1) Three coalescence modes can be observed using the DIC method: a shear coalescence mode, a tensile coalescence mode, and a mixed coalescence mode. (2) At the microscopic level, the bridge angle and crack arrangement affect the formation of the process zone; at the macroscopic level, they determine the crack propagation path and the failure mode. (3) The peak strength of the rock-like specimen is related to the crack inclination angle and the bridge angle. (4) Numerical modeling by the expanded distinct element method and the strain strength criterion simulates the different coalescence modes of the experimental study efficiently.

Keywords Rock-like material · Two parallel cracks · Rock bridge · Full-field strain · Failure evolution

List of Symbols

| | |
|----------------------|--|
| α | Crack inclination angle |
| β | Bridge angle |
| ε_t | Critical tensile strain |
| γ_{xycri} | Critical shear strain |
| σ_t | Critical tensile strength |
| σ_c | Critical compressive strength |
| σ_1, σ_3 | Maximum and minimum principal stresses, respectively |
| ν | Poisson's ratio |
| φ | Internal friction angle |
| c | Cohesion |

| | |
|--------------------------|--|
| C | Correlation coefficient |
| E | Young's modulus |
| G | Shear modulus |
| f_{1m}, f_{2m} | Average gray values of the reference and deformed images, respectively |
| $f_1(x, y), f_2(x', y')$ | Gray-level values for the reference and deformed images, respectively |
| f_t, f_s | Judgement factors of the tensile and shear cracks, respectively |

Abbreviations

| | |
|------|-----------------------------------|
| BPM | Bonded-particle model |
| DDM | Displacement discontinuity method |
| DEM | Discrete element method |
| DIC | Digital image correlation |
| EDEM | Expanded distinct element method |
| LEFM | Linear elastic fracture mechanics |
| PFC | Particle flow code |
| SIF | Stress intensity factor |
| SPZ | Shear process zone |
| TPZ | Tensile process zone |
| UDEC | Universal distinct element code |

✉ Cheng Zhao
zhaocheng@tongji.edu.cn
Yi meng Zhou
zhouyimeng52@163.com
Chun feng Zhao
tjzhchf@sohu.com
Chong Bao
baochong2006@163.com

¹ Key Laboratory of Geotechnical and Underground Engineering of Ministry of Education, Department of Geotechnical Engineering, Tongji University, Shanghai 200092, China

1 Introduction

Natural rock contains discontinuities, including pores, fractures, and inclusions or other defects, which govern the mechanical behavior of the rock mass (Li et al. 2010). The existence of discontinuities in the rock can decrease the strength and stiffness thereof and provide sources for the initiation of new discontinuities. In turn, these discontinuities may propagate and link with other cracks to further decrease the strength and the stiffness of the rock (Sagong and Bobet 2002). Therefore, it is necessary to investigate the fracture behavior of jointed rock. Numerous theoretical, experimental, and numerical studies have been carried out to study crack initiation, propagation, and coalescence in rocks (Hoek and Bieniawski 1965; Kranz 1983; Reyes and Einstein 1991; Park and Bobet 2009, 2010; Wong and Einstein 2006, 2009a, b, c; Haeri et al. 2014a, b; Zhang and Wong 2012, 2013, 2014).

The initial theoretical study of crack initiation and peak strength was conducted by Griffith (1921), who laid the foundation of fracture mechanics. Irwin (1957) modified Griffith's theory by considering plastic deformation and proposed the concept of the stress intensity factor (SIF). Dugdale (1960) studied the shapes of the plastic zones at crack tips. Horii and Nematnasser (1985) investigated the micromechanics of axial splitting and faulting. Furthermore, crack initiation criteria were comprehensively proposed by several scholars (Rice 1968; Bobet and Einstein 1998a, b; Park and Bobet 2010; Gonçalves and; Einstein 2013).

In terms of experimental study, Brace and Bombolakis (1963) first reported the propagation of tensile wing cracks from a pre-existing straight crack under uniaxial compression. Subsequently, Lajtai (1974) experimentally studied the strength of discontinuous rocks under direct shear loading and proposed the concept of wing cracks and secondary cracks. To incorporate the effect of friction, Shen et al. (1995) conducted experimental tests on gypsum specimens containing both open and closed cracks. Wong et al. (2001) analysis of rock-like materials containing three cracks showed that crack coalescence occurs between only two cracks and the lower value of coalescence stress dominates the coalescence process. Wong and Einstein (2006) investigated the cracking and coalescence behaviors of marble specimens. Furthermore, it was found that the geometry of pre-existing cracks dominates the initiation and coalescence behaviors of the specimen (Reyes and Einstein 1991; Park and Bobet 2009, 2010). Wong and Einstein (2009b, c) presented nine crack coalescence modes by considering various combinations of fundamental crack types. Haeri et al. (2014b) found that the strength of the specimens is adversely affected by the cracks, and

the peak strength of the specimen is related to the inclination angle of the cracks. Generally, significant advances were achieved in understanding coalescence modes and the effect of the interaction of pre-existing cracks on the behavior of each crack.

Compared with experimental study, numerical simulation is more convenient for obtaining mechanical information about cracks. In the past decades, various numerical studies have been conducted on different methods to research crack propagation and coalescence modes in specimens containing pre-existing cracks under compression (Petit and Barquins 1988; Bobet and Einstein 1998a, b; Jiang et al. 2009; Lan et al. 2010; Yang et al. 2013; Li and Wong 2014). Several numerical tools, such as DDM, FROCK, RFPA, PFC, and UDEC, have been developed for simulating different materials. Based on linear elastic fracture mechanics (LEFM) principles, the discrete code FROCK was developed by researchers at the Massachusetts Institute of Technology (MIT) to simulate cracking; this code performs in accordance with experimental observations (Chan 1986; Bobet and Einstein 1998a, b; Gonçalves and; Einstein 2013). Avoiding choosing a particular tip-based crack initiation criterion, an alternative approach based on the bonded-particle model (BPM) was used in many studies (Potyondy and Cundall 2004; Cho et al. 2007; Lee and Jeon 2011; Zhang and Wong 2012, 2013, 2014; Zhang et al. 2017). The BPM was shown to be able to simulate the cracking processes and failure of rock-like materials by simple interaction between particles. Tang et al. (2001) studied the crack coalescence modes in rock-like specimens containing three pre-existing cracks using RFPA^{2D}. Zhao et al. (2011) adopted the universal distinct element code (UDEC) to study the failure characteristic of brittle materials with an open hole. As a discrete element approach, the major advantage of using UDEC is that complex empirical constitutive behavior can be replaced by simple block contact logic and failure criterion. Zhang and Wong (2012) numerically studied the influence of the crack inclination angle on the cracking processes in brittle rock specimens containing a single crack. Wong and Li (2013) studied the coalescence of two coplanar cracks in a rock under compression using AUTODYN. Zhang et al. (2017) adopted BPM to investigate the acoustic emission characteristic of rock under different compression loading rates. These numerical studies have comprehensively promoted the understanding of crack initiation, propagation and coalescence mechanics.

It should be noted that with the updating of lab equipment and numerical methods, more and more experimental and numerical studies have been conducted on a micro level. The crack initiation, propagation and coalescence processes have been linked with acoustic emission, displacement field, and strain field in several researches (Tang et al. 2001; Lan et al. 2010; Lee and Jeon 2011; Wong and Li 2013; Zhang and

Wong 2014; Zhao et al. 2016; Zhang et al. 2017). Zhang and Wong (2014) introduced displacement trend lines to assist the analysis of the crack nature, and three types of displacement field were proposed. Zhao et al. (2016) used pairs of strain gauges to measure the deformation in both the axial and horizontal directions. Although the studies mentioned above have revealed the micro-cracking behaviors in rocks, due to the complications attributed to mineral composition, texture, and fabric, the cracking mechanism and details of the cracking processes are still need to be further studied. Moreover, the experimental investigations on the full-field strain concentration near the crack tips and rock bridge from a micro perspective are still not completely carried out. This paper aims to increase the understanding of the full-field strain by accurately recording the evolution strain diagrams during uniaxial compression loading and analyzing the stress–strain mechanical behaviors related to crack initiation, propagation and coalescence of a specimen with two parallel cracks.

This study adopts the digital image correlation (DIC) method, based on which the corresponding analysis codes are developed, to investigate the full-field strain concentration phenomenon during the cracking process. The rock-like material containing two parallel pre-existing cracks is under uniaxial compression. Two process zones, a shear process zone (SPZ) and a tensile process zone (TPZ), are defined according to the difference between high shear strain field and high tensile strain field. Moreover, the stress–strain curves of different specimens are systematically analyzed to enhance the understanding of the mechanical behavior of different coalescence modes. The peak strength related to different specimens is discussed. Furthermore, numerical studies are carried out with EDEM. Using the UDEC as the numerical tool, the present study efficiently simulates the coalescence modes of two pre-existing parallel cracks in rock under compression. The strain strength criterion is adopted in the numerical models to simulate the initiation of new cracks. The simulation results are generally in good accordance with experimental results.

2 Digital Image Correlation Method

The DIC method is an optical technique for full-field and non-contact measurement of deformations and strains of components and materials. It was originally developed by Peters and Ranson (1982) at the University of South Carolina. The basic principle of this method is the comparison of the digital images of the specimen surface in the undeformed (or reference) and deformed states by identifying the movement of a specific subset, as shown in Fig. 1. To identify the specific subset in two images, a grayscale function is used to represent the property of the subset. In addition, prior to

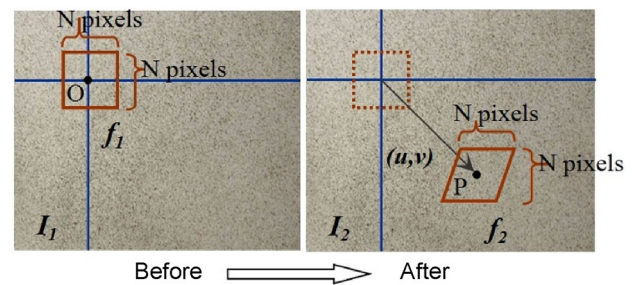


Fig. 1 Schematic diagram of the correlation match

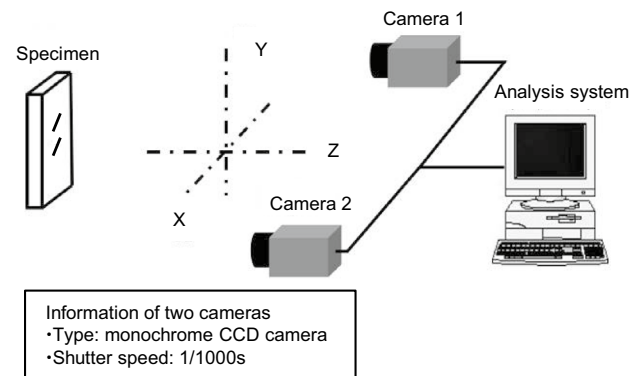


Fig. 2 Schematic of the DIC method

correlation analysis, a correlation coefficient C is defined as follows to evaluate the similarity between the reference and deformed subsets:

$$C = \frac{\sum [f_1(x, y) - f_{1m}] \cdot [f_2(x', y') - f_{2m}]}{\sqrt{\sum [f_1(x, y) - f_{1m}]^2} \sqrt{\sum [f_2(x', y') - f_{2m}]^2}}, \quad (1)$$

where $f_1(x, y)$ is the grayscale value at coordinate (x, y) for the reference image, $f_2(x', y')$ is the grayscale value at coordinate (x', y') for the deformed image, and f_{1m} and f_{2m} are the average gray values of the reference and deformed images, respectively.

The out-of-plane displacement should be removed from the analysis result when calculating the in-plane displacement. A 3D system is employed in the present study, as it yields high-precision results and calculates the out-of-plane displacement. As shown in Fig. 2, the 3D system uses two high-resolution digital cameras to record surface changes in the specimen as it deforms. The recorded images are correlated by applying the DIC method, which determines the object contours as well as the surface displacements. Taking into account the existence of noise points, the method of plane or curved fitting is used to address the displacement in the strain calculation. Considering the optical distortion, which can also affect the measured

result, the displacement field and strain field are modified to improve measurement precision.

For a comprehensive understanding of the DIC method for in-plane displacement and strain measurement, Pan et al. (2009) paper is highly recommended. Over the past few years, the DIC method has been improved significantly to reduce computation complexity, achieve highly accurate deformation measurements, and expand the application range. Moreover, numerous studies use the DIC method to investigate the failure of rock-like material (Zhao et al. 2011; Zhang et al. 2013).

3 Experimental Study

3.1 Specimen Preparation

Molded gypsum specimens are used to simulate rock behavior; they comprise a mixture of gypsum, water, and retarder in the ratio by weight of 1:0.2:0.005. Following considerable testing, the dimensions of the specimen are restricted to $100 \times 40 \times 10$ mm³. Owing to the small thickness, the crack does not rotate in the specimen. Thus, the surface crack path can represent the inner feature. In addition, the mechanical parameters of molded gypsum material are similar to those of rock (Table 1). The experimental results are compared with those from the previous iteration.

To generate two parallel pre-existing open cracks in the specimen, two smooth aluminum shims are placed in slots in the mold template and removed during curing. The positions and orientations of the slots are predetermined to create different combinations of crack inclination angle (α) and bridge angle (β). As shown in Fig. 3, the specimens have two parallel precracks with identical inclination angles (α), the crack length $2a$ in the specimens is 14 mm, and the bridge length $2b$ is 21 mm. α varies from 30° to 60° in 15° increments, and there are four β values: one equal to α and others of 90° , 120° , and 180° , as shown in Fig. 4. When the bridge angle is equal to the crack inclination angle, the two cracks are collinear. Owing to the boundary effect, the crack length and rock bridge length are scaled down to 10 and 15 mm, respectively. When the bridge angle is 90° , the bridge is vertical. When the bridge angle is 120° , two cracks are overlapping in the vertical direction. When the bridge angle is 180° , the two cracks are reversed. A coplanar bridge, a vertical bridge, overlapping cracks, and reverse cracks can be observed in the test to describe the cracking process. The bridge angles are determined in this way as a result of the coalescence modes.

Table 1 Specimen's parameters

| $a \times b \times c$ (mm ³) | σ_c (MPa) | σ_t (MPa) | E (MPa) | ν |
|--|------------------|------------------|-----------|-------|
| $100 \times 40 \times 10$ | 47.4 | 2.5 | 28,700 | 0.23 |

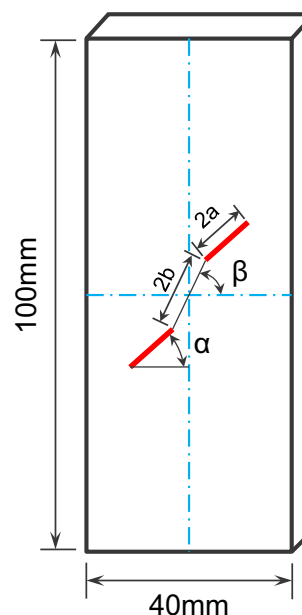


Fig. 3 Experimental specimen

3.2 Experimental Setup

The experimental setup consists of a loading machine, an observation system, and an analysis system (Fig. 5). The uniaxial compression is performed on a servo universal testing machine. The observation system includes two white light sources and two CCD cameras. The light sources are used to provide stable light during loading and observation. Two CCD cameras with a shutter speed of $1/1000$ s capture successive digital images of the specimen. Each pixel in the image is equal to 0.15 mm in the actual specimen. The analysis system code is developed on the basis of the DIC method principles, including the displacement analysis module, strain analysis module, and strain–displacement superposition module. By analyzing the images recorded by the cameras, the displacement and strain of the specimen surface can be obtained. Furthermore, this code has undergone innovation and optimization to increase the measurement accuracy. To avoid the computation of more than one target subregion, the code can expand the subregion automatically, compare it with the upper one, and achieve the best solution. Considering the existence of noise points in the calculation of deformation, the displacement field is fitted to a flat or a curved surface. To eliminate optical distortion of the test lens, the test lens is used to shoot an equidistant grid and then the revised parameter is calculated using the code. This code applies three-dimensional, as opposed to traditional two-dimensional, digital image technology to avoid the effect of the volume expansion and plane bending under rock compression on the accuracy of the plane displacement. It is easy to obtain the three-dimensional deformation of the

Fig. 4 Four bridge angles β in the specimen

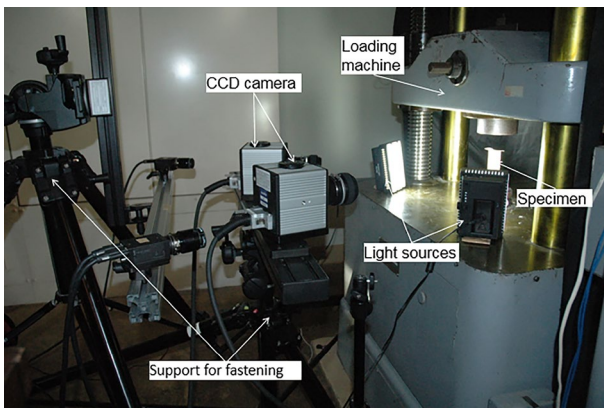
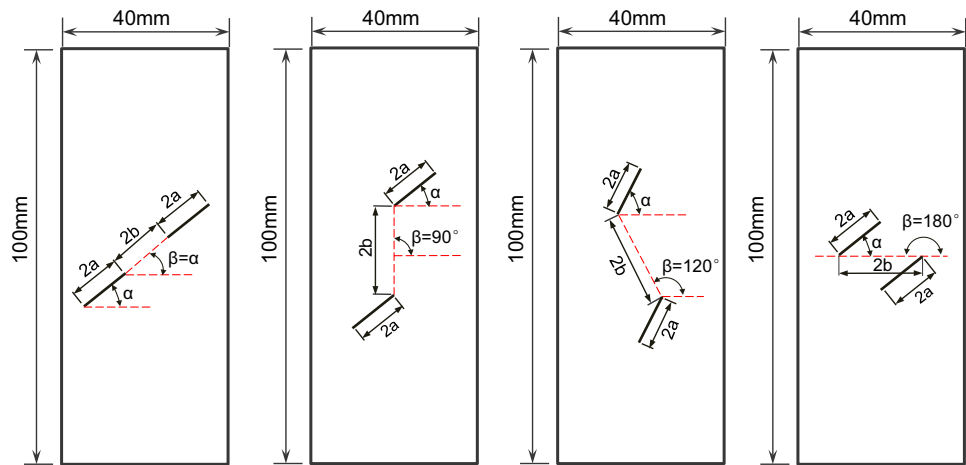


Fig. 5 Experimental setup

specimen by recording the loading process using two high-resolution digital cameras. To analyze the test results, the outer-plane data are used to study crack propagation.

3.3 Testing Procedure

Prior to placement in the loading machine, both specimen ends are covered with a piece of Teflon sheet daubed with butter. This arrangement reduces the friction between the specimen and the machine. Loading is carried out using displacement control at a rate of 0.02 mm/min. During the loading of the specimen, surface images are taken by two CCD cameras. All the loading information and digital images are transferred to the computer simultaneously. All specimens are loaded until either the cracks coalesce or the specimen fails, which is observed from a drop in the applied load. After test completion, the images are analyzed using a self-developed code. Crack slippage, initiation, and coalescence and failure stresses as well as the cracking process, coalescence mode, and crack type are studied at the meso-scale by analyzing the strain field and other experimental results.

4 Analysis of Experimental Results

By theoretical analysis, the strain approach observed in the DIC method is proved effective in investigating the cracking process and process zone. The characteristics of the cracking and damage evolution have been described in previous work (Zhao et al. 2015). Therefore, according to the tensile and shear properties of new cracks, two process zones are defined: the shear process zone (SPZ), which can be observed as an area with high shear strain concentration, and the tensile process zone (TPZ), which can be observed as an area with high tensile strain concentration. According to the second and third strength theories, ε_t and γ_{xyeri} can be defined as follows: $\varepsilon_t = \sigma_t/E$ and $\gamma_{xyeri} = \sigma_t/2G$, respectively. When the principal strain and the shear strain exceed the critical values, microcracks are considered to initiate. As a convenient description, the process zone contains the macrocrack area. Microcracks and macrocracks describe the propagation of cracks and the interaction of different cracks. New cracks coalesce in the bridge area and process zones coalesce. According to the integration modes of the TPZ and SPZ, three coalescence modes are defined based on the process zones observed in the DIC method: shear, tensile, and mixed coalescence. Shear coalescence means that the SPZs of two pre-existing cracks merge; tensile coalescence means that the TPZs of two pre-existing cracks merge; and mixed coalescence means that both the TPZs and SPZs of two pre-existing cracks merge. When the TPZs and SPZs of two pre-existing cracks do not merge, the failure process resembles single crack propagation.

As a convenient description, $\alpha - \beta$ represents the difference between the crack inclination angle α and the bridge angle β (Fig. 4). Therefore, representative specimens are selected to analyze the coalescence modes. The cracking process, coalescence properties, and failure properties are discussed based on the DIC strain field and the stress-strain curve. Figure 6 shows the failure crack pattern of these three

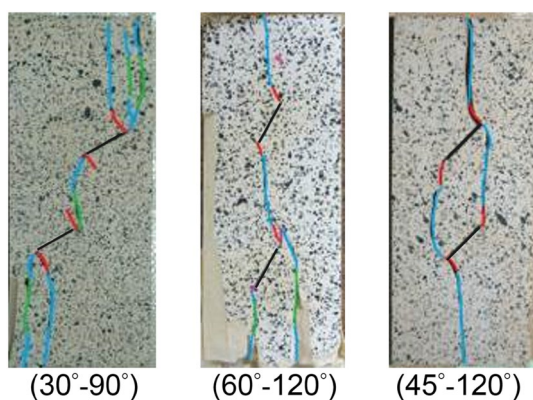


Fig. 6 Specimen failure photographs

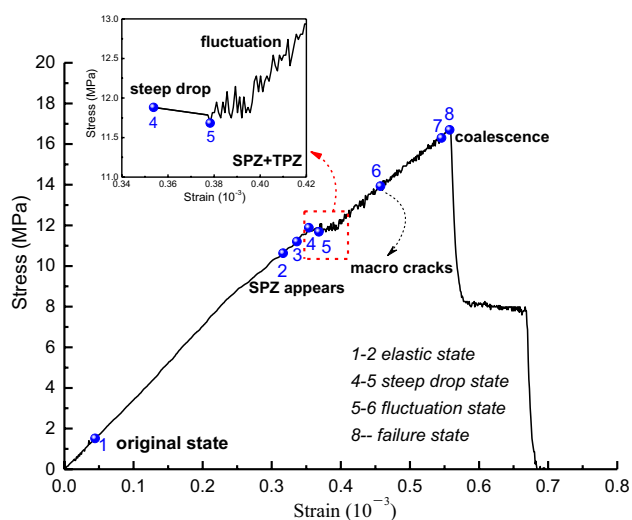


Fig. 7 Stress–strain curve of the loading process for the 30°–90° specimen

specimens. Specimen 30°–90° represents the shear coalescence mode; 60°–120°, the tensile coalescence mode; and 45°–120°, the mixed coalescence mode. “Inner tip” refers to the crack tip that is near the rock bridge, and “outer tip” refers to the crack tip that is away from the rock bridge.

4.1 Shear Coalescence

Figure 7 shows the stress–strain curve for the loading process. Figure 8 shows successive evolution diagrams of the principal strain and shear strain of the 30°–90° specimen at different loading stages obtained by the DIC system. Each stage of Fig. 8 is marked on the stress–strain curve in Fig. 7.

Stage 1 is the original state, which is used as a reference image for the remaining stages. As shown in the shear strain and principal strain diagrams of Stages 2 and 3, SPZs with approximately circular shapes appear on the surface of the

specimen with increasing load, especially at the tips of the two precracks. Moreover, the TPZ is not very clear. The principal strain value is low, and macrocracks do not initiate at this time. The stress–strain curve closely approximates a straight line, which indicates that the specimen’s mechanical behavior is elastic thus far. When the load is increased into Stages 4 and 5 (72.8% of the peak strength), the stress–strain curve exhibits a steep drop. It is found that the SPZs of the inner tips of the two precracks begin to merge and the TPZs of the two precracks develop independently in the load direction according to the strain diagrams. The macrocracks have not yet coalesced. This observation means that the merging of the process zones occurs before the macrocracks coalesce, and this phenomenon can cause the stress–strain curve to fluctuate. With increasing load, as shown in the figure for Stage 6, the SPZs in the shear strain diagram continue to merge, and the TPZs in the principal strain diagram merge gradually because of the macrocrack initiation. This result indicates that the shear mode crack in the bridge area is influenced by the tensile effect during the later stage. When the load reaches the peak strength, as shown in the diagrams of Stages 7 and 8, both the TPZs and the SPZs merge in the bridge area. The new cracks coalesce throughout the whole specimen, and the peak strength is 16.77 MPa. Compared with the failure photograph in Fig. 6, the new crack in the bridge area correlates well with the above analysis. Crack initiation, propagation, and coalescence result in strain redistribution and localization and fluctuation in the stress–strain curve. Although the crack in the bridge area is influenced by the tensile effect during the later stage, the main coalescence mode is shear coalescence.

4.2 Tensile Coalescence

Figure 9 shows the stress–strain curve for the loading process. Figure 10 shows successive evolution diagrams of principal strain and shear strain of the 60°–120° specimen at different loading stages obtained by the DIC system. Each stage of Fig. 10 is marked on the stress–strain curve in Fig. 9.

Stage 1 is the original state, used as a reference image for the remaining stages. As shown in the shear strain and principal strain diagrams of Stages 2 and 3, strain localization appears at the tips of the two precracks with increasing load. However, the strain is low. When the load is increased into Stages 4 and 5 (68.0% of the peak strength), the stress–strain curve exhibits a steep drop. The tensile strain figures show that TPZs appear gradually on the surface of the specimen, especially at the tips of the precracks, and the TPZs of the two precrack inner tips begin to merge. Observing the tensile strain figures, the SPZ is not very clear and only exists at the tip of the precrack. In accordance with the previous analysis, the merging of the process zones occurs before the macrocracks coalesce; this phenomenon can cause the

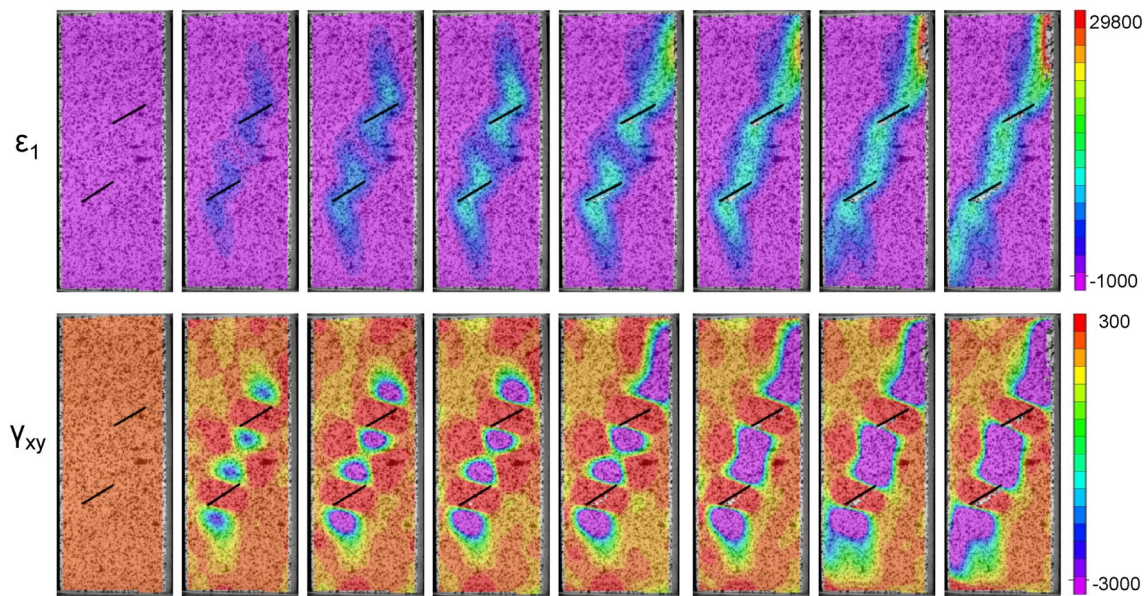


Fig. 8 Evolution diagrams of the principal strain and shear strain for the 30°–90° specimen

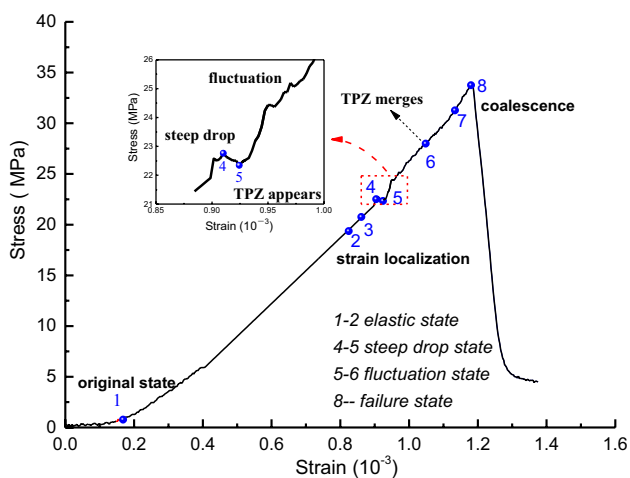


Fig. 9 Stress–strain curve of the loading process for the 60°–120° specimen

stress–strain curve to fluctuate. With increasing load, as shown in the diagrams for Stages 6 and 7, the TPZs in the principal strain diagram continue to merge, and the TPZ in the shear strain diagram is very small, although it increases gradually. Compared with the shear strain diagrams for the 30°–90° specimen, the strain value is considerably lower. When the load reaches the peak strength, as shown in the diagrams for Stage 8, only the TPZs merge, and the SPZ remains very small in the bridge area. The new cracks coalesce throughout the whole specimen. The peak strength is 33.9 MPa. Compared with the failure photograph in Fig. 6, the new crack in the bridge area correlates well with the

above analysis. Crack initiation, propagation, and coalescence result in strain redistribution and localization and fluctuation in the stress–strain curve. On the basis of the above analysis, the main coalescence mode is tensile coalescence.

4.3 Mixed Coalescence

Figure 11 shows the stress–strain curve for the loading process. Figure 12 shows successive evolution diagrams of principal strain and shear strain of the 45°–120° specimen at different loading stages obtained by the DIC system. Each stage of Fig. 12 is marked on the stress–strain curve in Fig. 11.

Stage 1 is the original state, used as a reference image for the remaining stages. As shown in the shear strain and principal strain diagrams of Stages 2 and 3, strain localization appears at the tips of the two precracks with increasing load. The stress–strain curve closely approximates a straight line, which indicates that the specimen's mechanical behavior is elastic thus far. When the load is increased into Stages 4 and 5 (82.0% of the peak strength), the stress–strain curve has a steep drop. The observation of the strain diagrams shows that SPZs and TPZs appear gradually on the surface of the specimen, especially at the tips of the precracks, and both of these zones begin to merge. The SPZs merge on the left side of the rock bridge area, and the TPZs merge on the right. The merging of the process zones also occurs before the macrocracks coalesce, and this phenomenon can cause the stress–strain curve to fluctuate. As the load continues to increase, as shown in the diagrams for Stages 6 and 7, the TPZs and SPZs continue to merge as the macrocrack propagates. This result indicates that

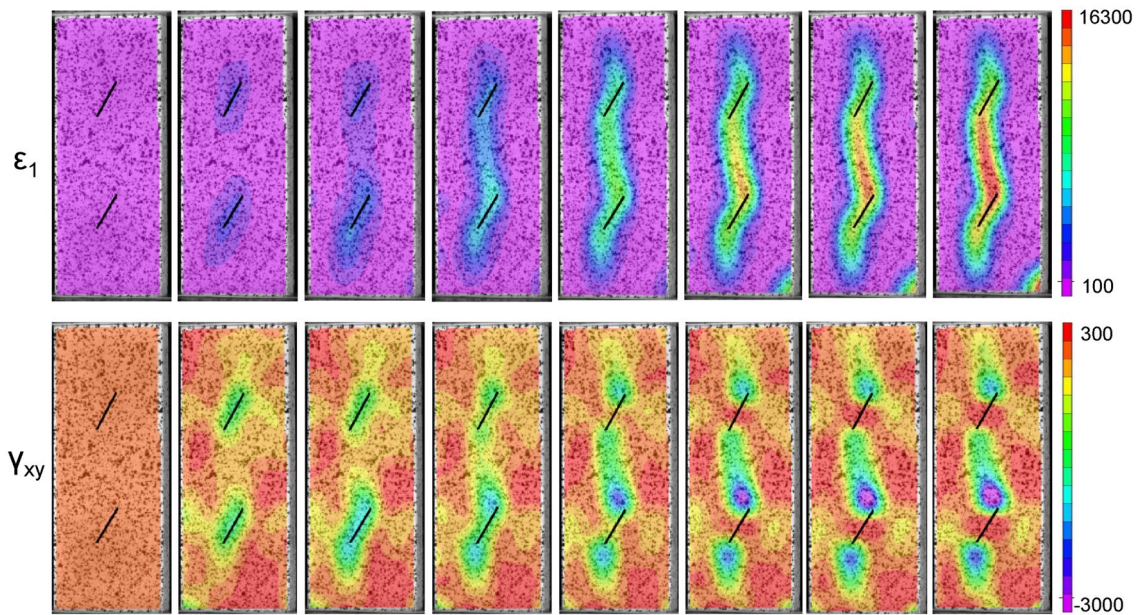


Fig. 10 Evolution diagrams of the principal strain and shear strain for the 60°–120° specimen

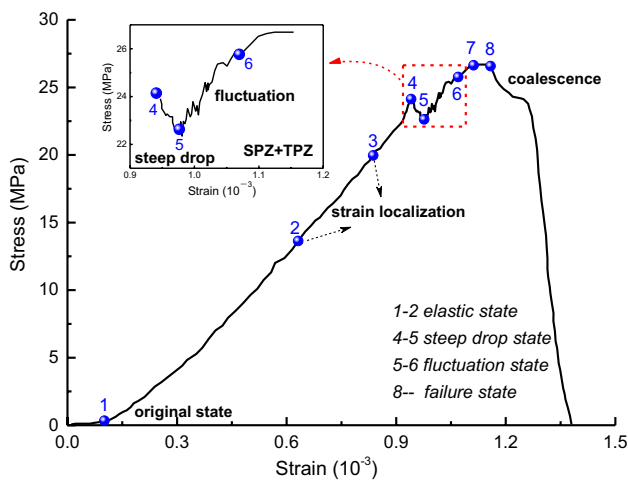


Fig. 11 Stress–strain curve of loading process of 45°–120° specimen

the failure of the specimen includes both shear stain coalescence and tensile strain coalescence. When the load reaches the peak strength, as shown in the diagrams for Stage 8, only the TPZs merge, and the SPZ remains very small in the bridge area. The new cracks coalesce throughout the whole specimen. The peak strength is 27.2 MPa. The peak strength is between those of the shear and tensile coalescence modes. Following this stage, the stress–strain curve near the peak strength has a step and then decreases rapidly. The specimen retains some structural resistance when the crack coalesces throughout the specimen. Compared with the failure photograph in Fig. 6, the new crack in the bridge area correlates well with the above analysis.

On the basis of the above analysis, the main coalescence mode is the mixed coalescence mode.

4.4 Peak Strength

The above discussion analyzes the failure pattern, the cracking process in the bridge area, and the stress–strain relationship in detail. To study the effects of the precrack inclination angle and the bridge angle on the peak strength, it is necessary to summarize the strength of all the specimens.

Figure 13 shows the peak strength with different bridge angles and precrack inclination angles. The horizontal coordinate axis is the bridge angle, and the vertical coordinate axis is the peak strength. The three curves represent the specimens with crack inclination angles of 30°, 45° and 60°. This figure shows that as the bridge angle increases, the peak strength of the specimens with the same inclination angle first decreases, then increases, and finally decreases. This fluctuation phenomenon is caused by the mechanical behaviors of the different coalescence modes. With the changes in the rock bridge, the strain localization areas reinforce or weaken each other, which leads to the differences in the peak strength. Moreover, when the bridge angle remains unchanged, the peak strength increases as the crack inclination angle increases. However, the 30°–30° specimen is a special case. When $\beta = \alpha$, the inclination angles corresponding to the peak strength in descending order are $\alpha = 60^\circ$, $\alpha = 30^\circ$, and $\alpha = 45^\circ$. As shown in Fig. 13, the TPZs of the 30°–30° specimen develop independently in the load direction according to

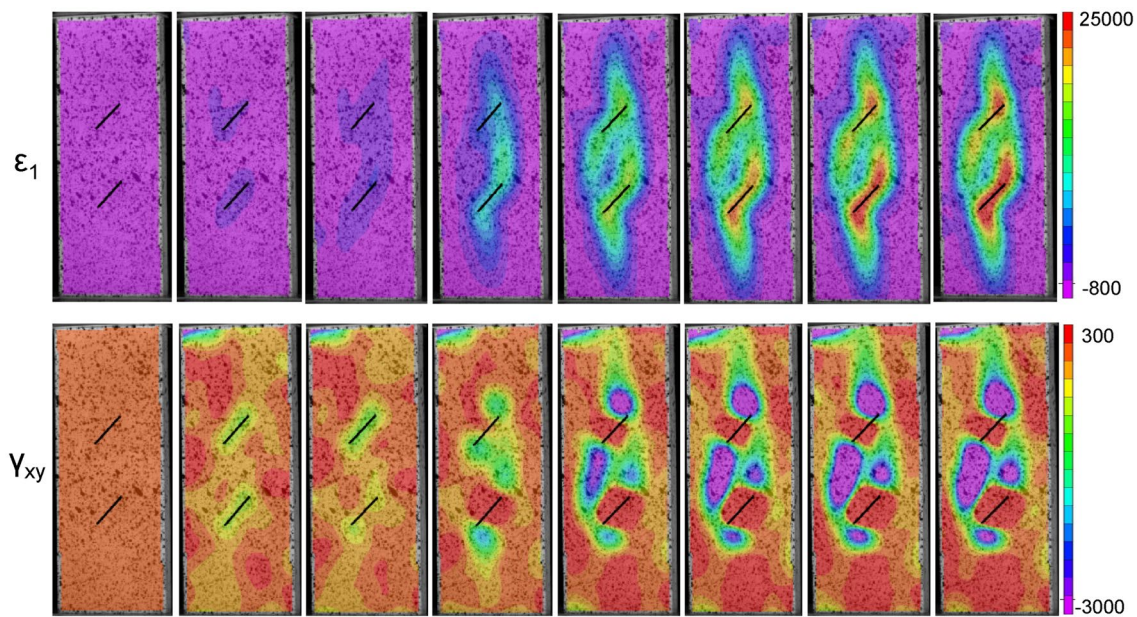


Fig. 12 Evolution diagrams of principal strain and shear strain of 45°–120° specimen

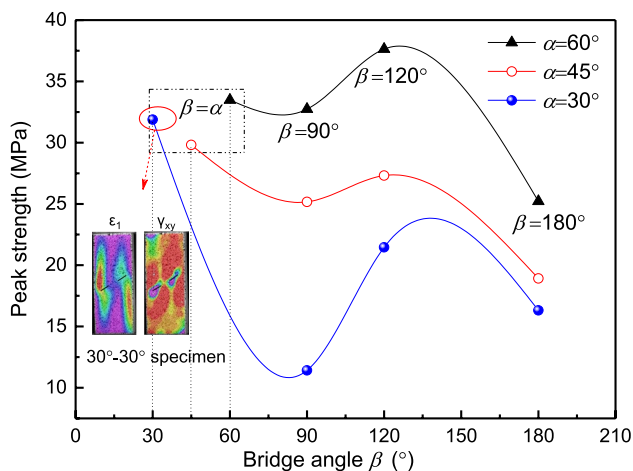


Fig. 13 Peak strength of different geometries

the principal strain diagram, and the SPZs of the 30°–30° specimen only exist at the tips of precracks according to the shear strain diagram. Neither the TPZs nor the SPZs merge in rock bridge area. Thus, macro coalescence does not occur, and the peak strength of the 30°–30° specimen is higher than that of the 45°–45° specimen. Apart from this case, the peak strength increases as the crack inclination angle increases, and this variation trend is similar to the experimental results on specimens with single cracks (Zhao et al. 2011). Therefore, it can be concluded that the peak strength is connected to the bridge angle and crack inclination angle.

5 Numerical Simulation

Cracks lead to the discontinuity and nonlinearity of the rock and cause opening, sliding, and other large deformation behaviors. Compared with experimental study, numerical simulation is more convenient for obtaining mechanical information about cracks (Wong and Li 2013). Among various numerical methods, the discrete element method (DEM), based on the assumption of discontinuous and large displacements, has inherent advantages in dealing with the problem of cracking. The DEM allows for finite displacement and rotation of the discrete bodies and can automatically identify new contacts in the calculation process. To better visualize the macroscopic crack development and simulate the cracking behaviors efficiently in parallel, this study adopts expanded distinct element method (EDEM) and numerical code UDEC to simulate the cracking processes.

To solve the problem of the initiation and propagation path of the macroscopic crack, the EDEM (Jiang et al. 2009) is adopted in the present study. This method provides a crack propagation path by setting up virtual cracks in all potential cracking areas. Both the virtual cracks and the blocks simulate the mechanical properties of the rock. When the equivalent stress state of the virtual crack satisfies the strength criterion, the virtual cracks are given the material parameters of real cracks, and a new crack initiates. To describe a tensile crack and a shear crack comprehensively, this paper employs an independent strain strength criterion (Zhao et al. 2017); it contains a tensile crack judgment criterion based on the principal strain and a shear crack judgment criterion based on the Mohr–Coulomb criterion. This strain strength

criterion assumes the following: (1) the tensile crack propagates in the direction of the maximum principal strain, and when the principal strain reaches a critical value (ε_t), the tensile crack initiates. (2) The shear crack propagates in the direction of the most dangerous stress state, and when the stress state Mohr circle is over the Mohr–Coulomb failure line, the shear crack initiates. The critical state expression is:

$$\begin{cases} \sigma_1 = (\sigma_3 + E\varepsilon_t)/\nu \\ \sigma_1 = 2c\sqrt{\frac{1 + \sin\varphi}{1 - \sin\varphi}} + \frac{1 + \sin\varphi}{1 - \sin\varphi}\sigma_3 \end{cases} \quad (2)$$

To apply the judgment of the tensile crack and shear crack to the numerical simulation, two crack judgment factors are defined:

$$f_t = \sigma_3 - \nu\sigma_1 + E\varepsilon_t, \quad (3)$$

$$f_s = \sigma_1 - \frac{1 + \sin\varphi}{1 - \sin\varphi}\sigma_3 - 2c\sqrt{\frac{1 + \sin\varphi}{1 - \sin\varphi}}, \quad (4)$$

where c is cohesion; φ is the internal friction angle; ε_t is the critical tensile strain; σ_1 and σ_3 are the principal stresses in the crack tip region when the pressure is positive; f_t is the judgment factor for the tensile crack and when $f_t > 0$, the tensile crack initiates; f_s is the judgment factor for the shear crack and when $f_s > 0$, the shear crack initiates.

The plane size of the specimen is $100 \times 40 \text{ mm}^2$ according to the laboratory test. To generate an appropriate number of discrete bodies, the specimen is cut into a collection of hexagonal blocks with side lengths of 1.5 mm by virtual cracks. The bridge angles and bridge lengths are the same as in the experiment, and the friction angle of the crack surface is 35° . The model of the numerical simulation is shown in Fig. 14; the loading plate on the top of the specimen is 10 mm, and the vertical displacement at the bottom of the specimen is fixed. The block follows the Mohr–Coulomb plasticity model ($\text{cons} = 3$), and a triangle mesh with a maximum edge less than 1 mm is generated in the interior. A contact–Coulomb sliding model is used for the crack surfaces ($\text{jcon} = 2$). The gravity stress is balanced prior to loading. The displacement boundary is loaded on the top of the specimen. Moreover, material parameters used in the simulation are provided in Table 2, and these parameters are obtained from the laboratory tests on the specimens (Zhao et al. 2017). Different colors are set in advance to represent cracks with different mechanical properties. All the specimens are simulated using the above method.

In agreement with the experimental analysis, three rock bridge coalescence modes can also be observed through the direct observation of the tensile and shear cracks in the numerical simulation results: shear coalescence, tensile

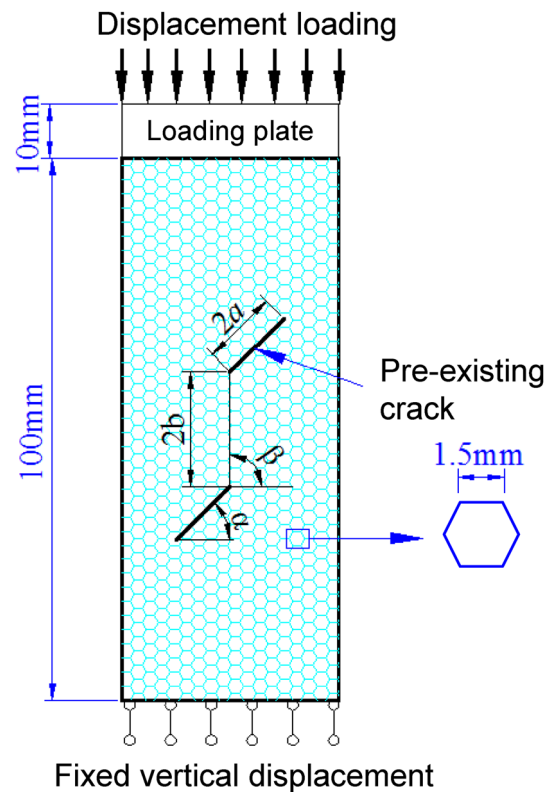


Fig. 14 Numerical model

coalescence, and mixed coalescence. After the simulation of the experimental specimens, the strength characteristics of the specimens with different rock bridge angles are analyzed. The crack inclination angle is 45° , and the bridge angle β varies from 0° to 180° in 22.5° increments. Meanwhile, combined with the numerical simulation results for different friction angles φ (0° , 17° , 27° , 35° , and 42°), the mechanisms of different bridge coalescence modes are studied. Consistent results are not achieved for the same specimen because of the difference between the numerical simulation method and the real material. Therefore, to study the general characteristics of all the coalescence modes more representatively, the typical specimen selected by numerical simulation is slightly different from the analyzed specimens that yield the laboratory experimental results. From the general rules of the different coalescence modes, the results of the numerical simulation reflect the experimental phenomena very well. This result provides a basis for the in-depth study of the coalescence modes from a numerical aspect.

5.1 Shear Coalescence

Figure 15 shows the evolution diagrams for the crack propagation in a typical specimen with the shear coalescence mode. It can be seen that following crack initiation, the propagation rate of the precracks' inner tips is larger than

that of the outer ones. Within a short period after initiation, the shear cracks of the precracks' inner tips merge; shear crack coalescence occurs in the rock bridge region. This outcome is consistent with the results of the shear coalescence mode using the DIC method.

To analyze the mechanism of shear coalescence in the bridge area of the specimen with two parallel cracks, Fig. 16 shows the evolution diagrams of the horizontal displacement

field and the shear stress field in the numerical simulation. It can be seen from the horizontal displacement field that the anti-symmetric axis of the horizontal displacement field of the rock bridge is a broken line in the early stages of the experiment; this line is not coincident with the connection of the precracks' inner tips. However, when the shear cracks initiate, the anti-symmetric axis becomes a straight line and is coincident with the connection of the rock bridge. The slip

Table 2 Material parameters of expanded distinct element model

| Parameters | Block | Pre-existing crack | Virtual crack | New crack |
|-----------------------------------|-----------------------|-----------------------|-----------------------|-----------------------|
| Density d (kg/m) | 1810.00 | – | – | – |
| Bulk modulus K (Pa) | 7.41×10^{10} | – | – | – |
| Shear modulus G (Pa) | 4.88×10^{10} | – | – | – |
| Normal stiffness k_n (Pa/m) | – | 1.60×10^{13} | 1.60×10^{13} | 4.00×10^{11} |
| Tangential stiffness k_s | – | 8.00×10^{12} | 1.60×10^{13} | 2.00×10^{11} |
| Cohesion c (Pa) | 1.80×10^7 | 0 | 1.00×10^{10} | 0 |
| Internal friction angle φ | 25.60 | 35.00 | 80.00 | 15.00 |
| Tensile strength σ_t (Pa) | 1.50×10^7 | 0 | 1.00×10^{10} | 0 |
| Dilation angle ($^\circ$) | 0 | 0 | 0 | 0 |

Fig. 15 Evolution diagrams of crack propagation in shear coalescence mode for the numerical simulation (60° – 60° specimen)

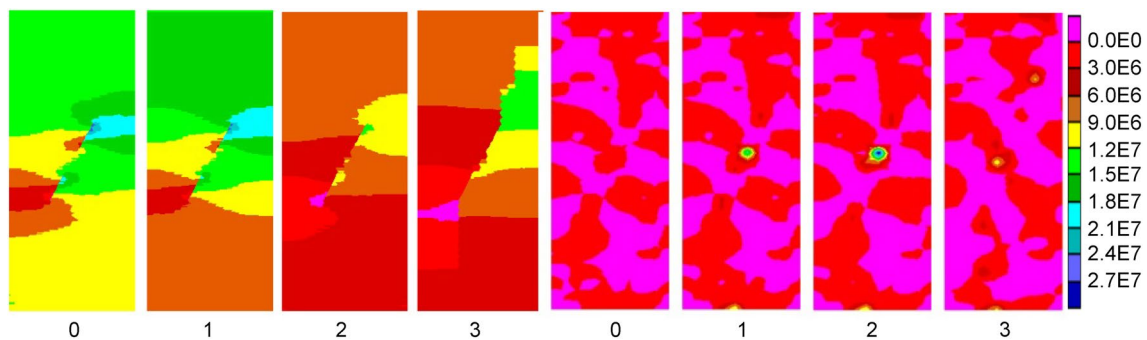
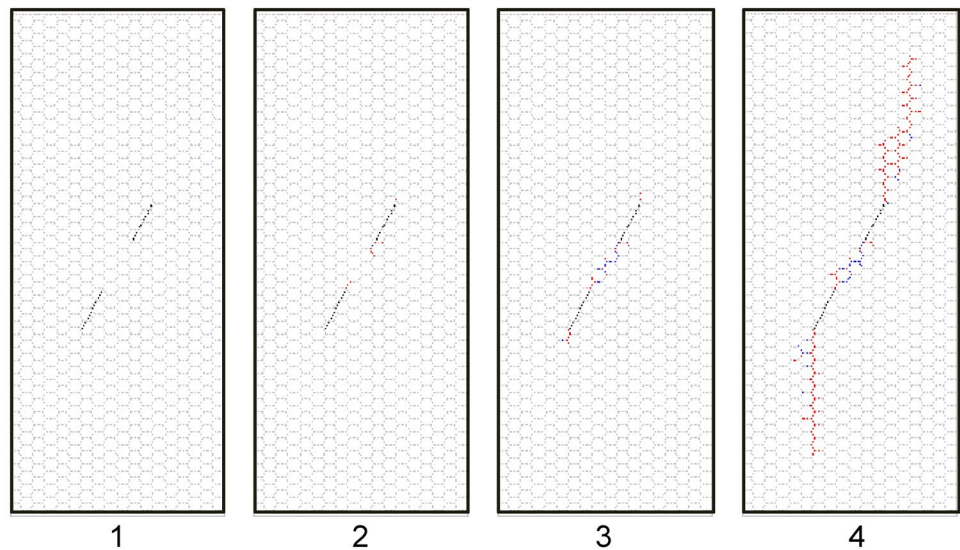


Fig. 16 Evolution diagrams of the horizontal displacement field and the shear stress field for the numerical simulation (60° – 60° specimen)

on both sides of the rock bridge intensifies the further propagation of the shear crack, which leads to the occurrence of shear coalescence. Analysis of the diagrams of the shear stress field: following crack initiation, the stress fields of the crack tips interfere with each other, which causes stress concentration in the rock bridge area (Identification point 1). With crack propagation, the shear stress concentration strengthens gradually (Identification point 2). With shear stress, slip failure appears on the both sides of the bridge, resulting in the shear coalescence mode.

5.2 Tensile Coalescence

Figure 17 shows the evolution diagrams for the crack propagation in a typical specimen with the tensile coalescence mode; it can be seen that the new cracks initiate at the precracks' inner and outer tips. The new cracks are mainly tensile cracks; shear cracks propagate slowly. At Identification point 3, the tensile cracks of the precracks'

inner tips propagate unsteadily and suddenly coalesce across the whole bridge area. This outcome is consistent with the results of the tensile coalescence mode using the DIC method.

To analyze the mechanism of tensile coalescence in the bridge area of the specimen with two parallel cracks, Fig. 18 shows the evolution diagrams of the principal stress field and the tensile stress distribution in the numerical simulation. In the initial loading stage, a stress concentration is generated at the crack tip. At the critical coalescence time (Identification point 2), compared to the crack initiation time (Identification point 1), the extension of the tensile crack length is shorter, but the tensile stress concentration degree and the distribution range increase greatly. Thereafter, the rock bridge suddenly coalesces, with stress release (Identification point 3). Therefore, the tensile stress sustained accumulation phenomenon is the poised stage of tensile coalescence; it is also the main reason for the sudden coalescence.

Fig. 17 Evolution diagrams of crack propagation in tensile coalescence mode for the numerical simulation (60° – 90° specimen)

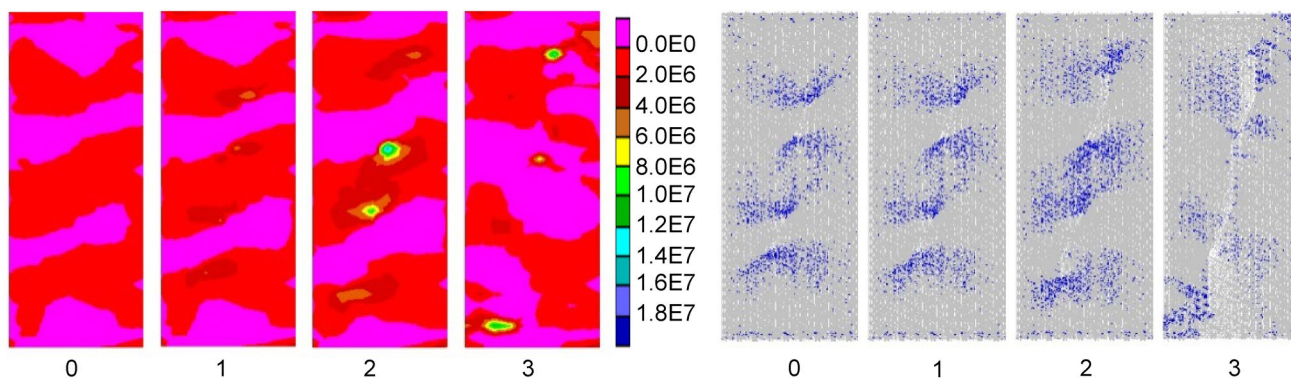
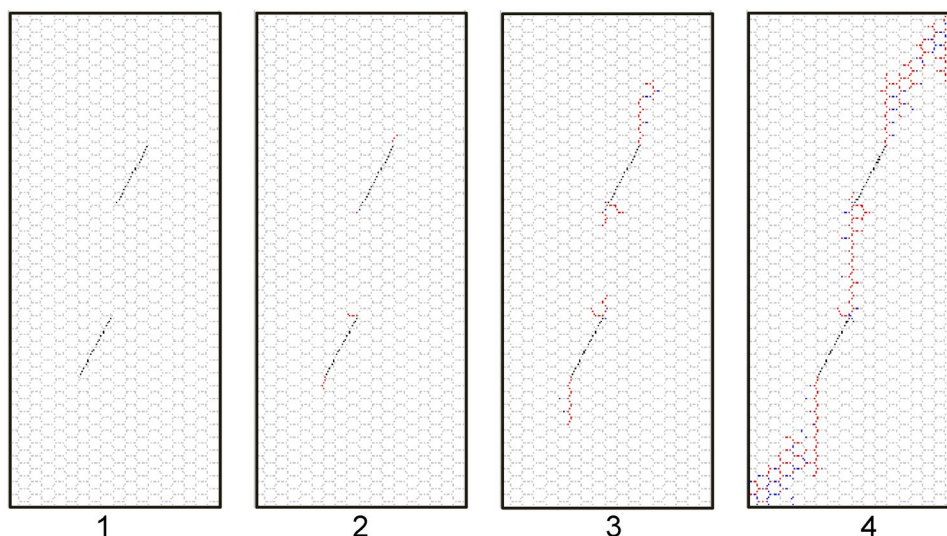


Fig. 18 Evolution diagrams of the principal stress field and the tensile stress distribution for the numerical simulation (60° – 90° specimen)

Fig. 19 Evolution diagrams of crack propagation in mixed coalescence mode for the numerical simulation (45° – 120° specimen)

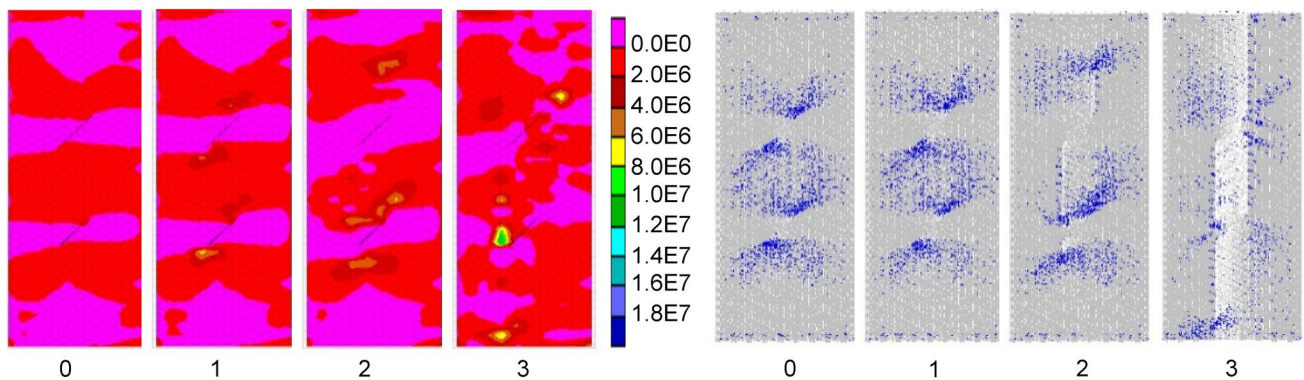
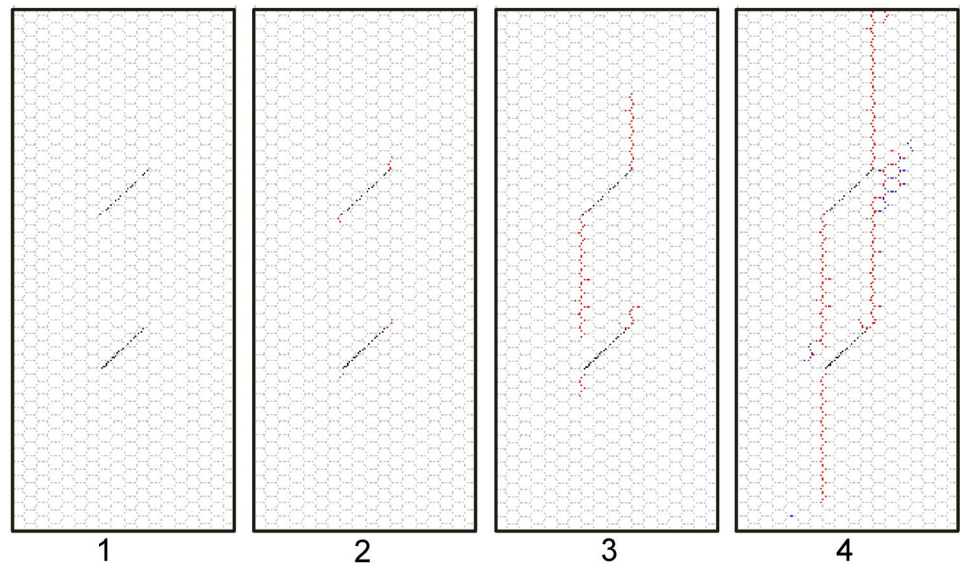


Fig. 20 Evolution diagrams of the principal stress field and the tensile stress distribution for the numerical simulation (45° – 120° specimen)

5.3 Mixed Coalescence

Figure 19 shows the evolution diagrams for the crack propagation in a typical specimen with the mixed coalescence mode; it can be seen that the new cracks initiate at the pre-cracks' inner and outer tips. When the tensile cracks are about to coalesce across the bridge, these cracks merges with shear cracks (anti-wing cracks) at the cracks' tips. The rock bridge area coalesces. This outcome is consistent with the results of the mixed coalescence mode using the DIC method.

To analyze the mechanism of mixed coalescence in the bridge area of the specimen with two parallel cracks, Figs. 20 and 21 show the evolution diagrams of the principal stress field, the changes in the tensile stress distribution, and the evolution diagrams of the shear stress field. It can be seen from the diagrams that the tensile stress concentration at the crack tips at initial loading and the interference occur in the rock bridge area. However, the anti-wing cracks area

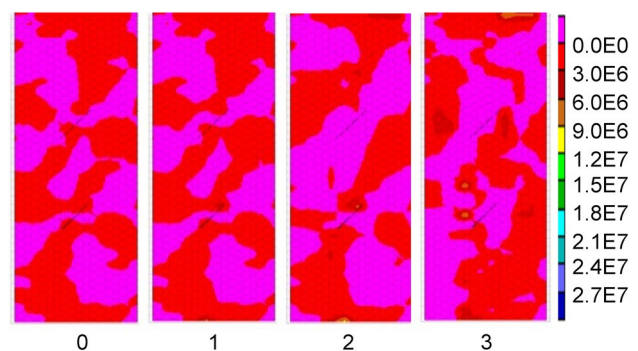


Fig. 21 Evolution diagrams of the shear stress field for the numerical simulation (45° – 120° specimen)

of the crack tips are compressed; thus, the cracks are arrested when the tensile cracks propagate to the surrounding areas. Following this stage, the shear stress concentration in the anti-wing crack zone can be observed in the shear strain

diagrams. Tensile cracks caused by tensile stress concentration and shear cracks caused by shear stress concentration coalesce together across the bridge area.

5.4 Other Factors

According to the previous studies, the influence of crack arrangements and internal friction coefficients on coalescence modes and strength properties of the specimens are classic problems and have been studied extensively (Wong and Chau 1998; Wong and Einstein 2009b, c; Li and Ma 2009; Park and Bobet 2010; Wong and Li 2013). Using UDEC as the numerical tool, the present study has systematically simulated the coalescence mode and peak strength of specimens with different bridge angles and friction coefficients. The strain strength criterion is adopted in the numerical models to simulate the initiation, propagation, and coalescence processes of new cracks. In this section, the effects of different bridge angles and crack surface friction angles on the strength properties and coalescence modes are studied by the numerical method. To control the variables, the crack length and bridge length are defined. The crack length is 10 mm; the bridge length is 12 mm. These values ensure not only that the rock bridge angle is small (there remains a distance from the crack boundary of the specimen) but also that the adjustment of the bridge length can be realized.

5.4.1 Analysis of Different Bridge Angles

The bridge angle β varies from 0° to 180° in 22.5° increments, the crack inclination angle α is 45° , and the friction angle of the crack surface is 35° . The results of the numerical simulation are consistent with the mechanisms of the three coalescence modes described above. However, when the bridge angle is too small (0° and 22.5°) or too large (157.5° and 180°), coalescence does not occur. When the bridge angle is small, there are two anti-symmetric regions of the horizontal displacement field on both sides of the rock bridge as a crack initiates. With the continuous propagation of wing cracks, the two regions are gradually integrated, which inhibits the initiation of shear cracks in the rock bridge; therefore, shear coalescence does not occur. The principal stress field can be obtained experimentally: in the initial stage of loading, the stress fields of the two cracks interfere with each other in the rock bridge; the tensile concentration is not high in the bridge. With the propagation of wing cracks, the rock bridge becomes compressed; therefore, when the bridge angle is small, tensile coalescence does not occur. When the bridge angle is large, it is found that the bridge is mainly compressed according to the diagrams of principal stress and tensile stress; in contrast, the tensile stress is highly concentrated at the outer tip. Thus, coalescence cannot occur in the bridge. Then, the strength

characteristics of specimens with different rock bridge angles are studied. Figure 22 shows the peak strength of the different specimens and several bridge coalescence modes. It can be seen that the bridge angle affects not only the crack coalescence mode but also the peak strength of the specimens. This observation is consistent with the experimental results. With the change of the bridge angle from 0° to 180° , the strength of the specimen first increases and then decreases, then increases again, and finally decreases. The strength is the lowest when the bridge angle is 90° , and the tensile coalescence mode occurs at this time. Tensile cracks are generated earlier than shear cracks under uniaxial compression, and following tensile coalescence, the stress–strain curve reaches the peak value very quickly; thus, the strength decreases. The strengths of the shear coalescence mode and non-coalescence mode are higher. Owing to the crack characteristics and the generation mechanism, the strength of the mixed coalescence mode is in between those of the tensile and shear coalescence modes. The peak strength curve obtained by the numerical method is consistent with Wang and Chau's (1998) experimental results.

5.4.2 Analysis of Different Friction Angles

The mixed coalescence mode occurs in a 45° – 67.5° specimen. Thus, the study of the mechanical characteristics of this specimen is more significant for reference because of the appearance of tensile and shear cracks. Select 67.5° as the reference bridge angle; change only the crack surface friction angle (0° , 17° , 24° , 35° , and 42°). A numerical simulation is used to study the effects of different crack friction angles on the crack propagation in and the strength of the specimen. Figures 23 and 24 show the crack propagation path, peak strength, and coalescence stress of the specimens

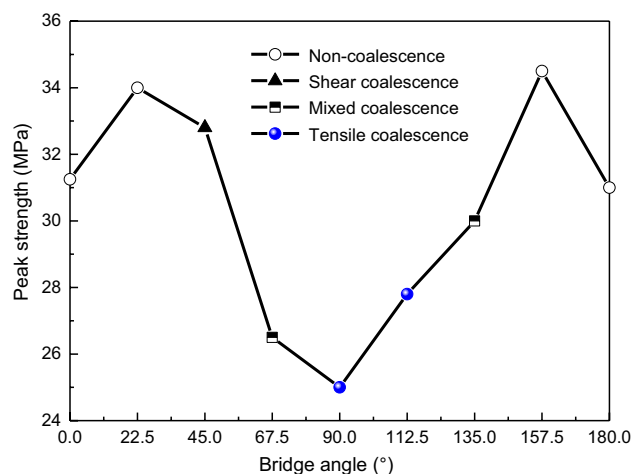


Fig. 22 Peak strength and coalescence modes for different bridge angles ($\alpha = 45^\circ$)

with different friction angles. Several conclusions can be drawn from these figures.

From the aspect of the mechanical properties of the specimen, the larger the friction angle is, the more obvious the shear characteristics of the specimen. When the friction angle is small (0° , 17° , and 27°), tensile cracks dominate the failure. When the friction angle is large (35° and 42°), tensile and shear cracks dominate the failure together. When considering the crack surface friction effect, crack propagation needs not only to provide the surface energy but also to overcome the energy loss caused by the friction effect. Therefore, the resistance of the specimen increases, the crack propagation process is prolonged, and the shear crack is more easily propagated under high stress.

From the aspect of the coalescence properties of the rock bridge, when the friction angle is small (0° , 17° , and 27°), the wing cracks at the inner tips merge; when the friction angle is large (35° and 42°), the wing cracks at the inner tips merge by shear cracks. Thus, with increasing friction angle, the coalescence mode slowly changes from tensile coalescence to mixed coalescence.

From the aspect of the strength properties, with the increase in the friction angle, the coalescence stress first increases and then becomes stable; the peak strength increases gradually, and the ratio of coalescence stress to peak strength increases. This numerical result is consistent with the previous experimental studies (Wong and Chau 1998; Park and Bobet 2010). When the friction angle is small (0° , 17° , and 27°), the coalescence stress increases with increasing friction angle, the coalescence stress is the same as the peak strength, and the specimen shows brittle failure. When the friction angle is large (35° and 42°), although the coalescence stress remains unchanged, the peak strength increases with the larger friction angle; this result shows that the failure process of the specimen increases ductility.

Fig. 23 Diagrams of crack propagation of the specimen with different friction angle (45° – 67.5° specimen)

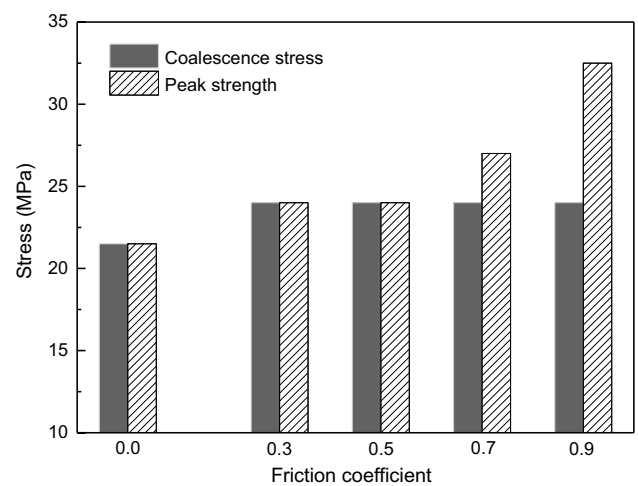
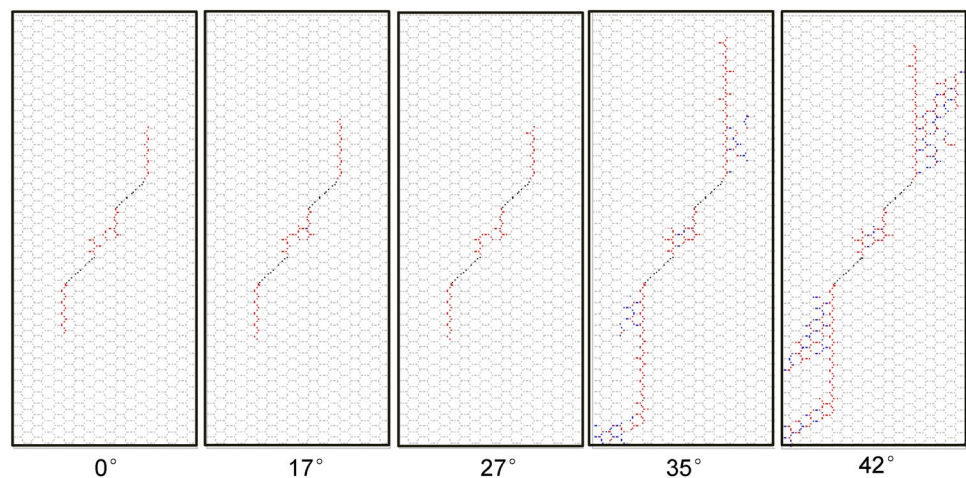


Fig. 24 Strength of the specimen with different friction angles (45° – 67.5° specimen)

6 Conclusions

In this study, the full-field strain and coalescence modes of rock-like materials with two parallel cracks under uniaxial compression are experimentally studied using the DIC method. The specimens used in this study have different geometries (inclination angle and bridge angle). Two process zones are defined according to the investigation of the high strain concentration area, and representative specimens are discussed in terms of the strain approach and process zone to clarify three coalescence modes. Moreover, numerical studies are carried out on the basis of the EDEM. Using the distinct element code UDEC as the numerical tool, the present study efficiently simulates the coalescence modes of two pre-existing parallel cracks in a rock under compression. The strain strength criterion is adopted in the numerical models to simulate the

initiation of new cracks. The simulation results are generally in good accordance with the experimental results. The specific conclusions are as follows:

1. Two process zones can be defined by the high strain field obtained by the DIC method: a shear process zone (SPZ), which can be observed as high shear strain concentration, and a tensile process zone (TPZ), which can be observed as high tensile strain concentration. Three coalescence modes can be found: a shear coalescence mode, a tensile coalescence mode, and a mixed coalescence mode. The shear coalescence mode means that the SPZs of two pre-existing cracks merge. The tensile coalescence mode means that the TPZs of two pre-existing cracks merge. Mixed coalescence means that both the TPZs and SPZs of two pre-existing cracks merge.
2. The stress–strain curves for different coalescence modes are systematically studied. It is found that the stress–strain curves have four typical stages—elastic stage, steep drop stage, fluctuation stage, and coalescence stage. Furthermore, the merging of the process zones occurs before the macrocracks coalesce, and this phenomenon can cause the stress–strain curve to fluctuate.
3. The peak strength is related to the bridge angle as well as the crack inclination angle. As the bridge angle increases, the peak strength of the specimens with the same inclination angle first decreases, then increases, and finally decreases. When the bridge angle remains unchanged, the peak strength increases with increasing crack inclination angle, except for non-coalescence specimens.
4. Numerical modeling by the expanded distinct element method and the strain strength criterion efficiently simulates the different coalescence modes (shear coalescence, tensile coalescence, and mixed coalescence) of the experimental study. The bridge angle affects not only the crack coalescence mode but also the peak strength of the specimen. Moreover, when the friction angle of the crack surface increases gradually, the shear failure characteristics of the specimen are increasingly obvious, and the coalescence mode slowly changes from tensile coalescence to mixed coalescence. The peak strength increases gradually, and the ratio of coalescence stress to peak strength increases.

Acknowledgements The authors would like to acknowledge the financial support of the National Key R&D Program of China (no. 2017YFC0806000), the National Natural Science Foundation of China (nos. 41202193 and 41572262), the Innovation Program of the Shanghai Municipal Education Commission (no. 15ZZ016), and the Shanghai Rising-Star Program (no. 17QC1400600).

Compliance with ethical standards

Conflict of interest No potential conflicts of interests were reported by the authors.

References

- Bobet A, Einstein HH (1998a) Fracture coalescence in rock-type materials under uniaxial and biaxial compression. *Int J Rock Mech Min Sci* 35(7):863–888. [https://doi.org/10.1016/S0148-9062\(98\)00005-9](https://doi.org/10.1016/S0148-9062(98)00005-9)
- Bobet A, Einstein HH (1998b) Numerical modeling of fracture coalescence in a model rock material. *Int J Fract* 92(33):221–252. <https://doi.org/10.1023/A:1007460316400>
- Brace WF, Bombolakis EG (1963) A note on brittle crack growth in compression. *J Geophys Res* 68(12):3709–3713
- Chan HCM (1986) Automatic two-dimensional multi-fracture propagation modelling of brittle solids with particular application to rock. Dissertation, Massachusetts Institute of Technology
- Cho N, Martin CD, Sego DC (2007) A clumped particle model for rock. *Int J Rock Mech Min Sci* 44(7):997–1010
- Dugdale DS (1960) Yielding of steel sheets containing slits. *J Mech Phys Solids* 8(2):100–104. [https://doi.org/10.1016/0022-5096\(60\)90013-2](https://doi.org/10.1016/0022-5096(60)90013-2)
- Goncalves da Silva B, Einstein HH (2013) Modeling of crack initiation, propagation and coalescence in rocks. *Int J Fract* 182(2):167–186. <https://doi.org/10.1007/s10704-013-9866-8>
- Griffith AA (1921) The phenomena of rupture and flow in solids. *Philos Trans R Soc* 221(582–593):163–198
- Haeri H, Shahriar K, Marji MF, Moarefvand P (2014a) On the strength and crack propagation process of the pre-cracked rock-like specimens under uniaxial compression. *Strength Mater* 46(1):140–152. <https://doi.org/10.1007/s11223-014-9525-y>
- Haeri H, Shahriar K, Marji MF, Moarefvand P (2014b) Experimental and numerical study of crack propagation and coalescence in pre-cracked rock-like disks. *Int J Rock Mech Min Sci* 67:20–28. <https://doi.org/10.1016/j.ijrmms.2014.01.008>
- Hoek E, Bieniawski ZT (1965) Brittle fracture propagation in rock under compression. *Int J Fract* 1(3):137–155
- Horii H, Nematnasser S (1985) Compression-induced microcrack growth in brittle solids: axial splitting and shear failure. *J Geophys Res Sol Earth* 90(NB4):3105–3125. <https://doi.org/10.1029/JB090iB04p03105>
- Irwin GR (1957) Relation of stresses near a crack to the crack extension force. 9th International congress of applied mechanics, Brussels, pp 245–251
- Jiang YJ, Li B, Yamashita Y (2009) Simulation of cracking near a large underground cavern in a discontinuous rock mass using the expanded distinct element method. *Int J Rock Mech Min Sci* 46(1):97–106. <https://doi.org/10.1016/j.ijrmms.2008.05.004>
- Kranz RL (1983) Microcracks in rocks—a review. *Tectonophysics* 100(1–3):449–480. [https://doi.org/10.1016/0040-1951\(83\)90198-1](https://doi.org/10.1016/0040-1951(83)90198-1)
- Lajtai EZ (1974) Brittle fracture in compression. *Int J Fract* 10(4):525–536
- Lan H, Martin CD, Hu B (2010) Effect of heterogeneity of brittle rock on micromechanical extensile behavior during compression loading. *J Geophys Res* 115:B01202. <https://doi.org/10.1029/2009JB006496>
- Lee H, Jeon S (2011) An experimental and numerical study of fracture coalescence in pre-cracked specimens under uniaxial compression. *Int J Solids Struct* 48(6):979–999. <https://doi.org/10.1016/j.ijsolstr.2010.12.001>

- Li JC, Ma GW (2009) Experimental study of stress wave propagation across a filled rock joint. *Int J Rock Mech Min Sci* 46(3):471–478. <https://doi.org/10.1016/j.ijrmms.2008.11.006>
- Li HQ, Wong LNY (2014) Numerical study on coalescence of pre-existing flaw pairs in rock-like material. *Rock Mech Rock Eng* 47(6):2087–2105. <https://doi.org/10.1007/s00603-013-0504-6>
- Li JC, Ma GW, Zhao J (2010) An equivalent viscoelastic model for rock mass with parallel joints. *J Geophys Res Sol Earth*. <https://doi.org/10.1029/2008JB006241>
- Pan B, Qian KM, Xie HM, Asundi A (2009) Two-dimensional digital image correlation for in-plane displacement and strain measurement: a review. *Meas Sci Technol*. <https://doi.org/10.1088/0957-0233/20/6/062001>
- Park CH, Bobet A (2009) Crack coalescence in specimens with open and closed flaws: a comparison. *Int J Rock Mech Min Sci* 46(5):819–829. <https://doi.org/10.1016/j.ijrmms.2009.02.006>
- Park CH, Bobet A (2010) Crack initiation, propagation and coalescence from frictional flaws in uniaxial compression. *Eng Fract Mech* 77(14):2727–2748. <https://doi.org/10.1016/j.engfracmec.2010.06.027>
- Peters WH, Ranson WF (1982) Digital imaging techniques in experimental stress-analysis. *Opt Eng* 21(3):427–431. <https://doi.org/10.1117/12.7972925>
- Petit JP, Barquins M (1988) Can natural faults propagate under mode II conditions. *Tectonics* 7(6):1243–1256. <https://doi.org/10.1029/TC007i006p01243>
- Potyondy DO, Cundall PA (2004) A bonded-particle model for rock. *Int J Rock Mech Min Sci* 41(8):1329–1364
- Reyes O, Einstein HH (1991) Failure mechanisms of fractured rock: a fracture coalescence model. 7th ISRM congress, Aachen, pp 333–340
- Rice JR (1968) A path independent integral and the approximate analysis of strain concentration by notches and cracks. *Int J Appl Mech* 35(2):379–386. <https://doi.org/10.1115/1.3601206>
- Sagong M, Bobet A (2002) Coalescence of multiple flaws in a rock-model material in uniaxial compression. *Int J Rock Mech Min Sci* 39(2):229–241. [https://doi.org/10.1016/S1365-1609\(02\)00027-8](https://doi.org/10.1016/S1365-1609(02)00027-8)
- Shen BT, Stephansson O, Einstein HH, Ghahreman B (1995) Coalescence of fractures under shear stresses in experiments. *J Geophys Res Sol Earth* 100(B4):5975–5990. <https://doi.org/10.1029/95JB00040>
- Tang CA, Lin P, Wong RHC et al (2001) Analysis of crack coalescence in rock-like materials containing three flaws-part 2: numerical approach. *Int J Rock Mech Min Sci* 38:925–939
- Wong RHC, Chau KT (1998) Crack coalescence in a rock-like material containing two cracks. *Int J Rock Mech Min Sci* 35(2):147–164. [https://doi.org/10.1016/S0148-9062\(97\)00303-3](https://doi.org/10.1016/S0148-9062(97)00303-3)
- Wong LNY, Einstein HH (2006) Fracturing behavior of prismatic specimens containing single flaws. In: Proceedings of the 41st US symposium on rock mechanics, Golden, Colorado, ARMA/USRMS 06-899
- Wong LNY, Einstein HH (2009a) Systematic evaluation of cracking behavior in specimens containing single flaws under uniaxial compression. *Int J Rock Mech Min Sci* 46(2):239–249. <https://doi.org/10.1016/j.ijrmms.2008.03.006>
- Wong LNY, Einstein HH (2009b) Crack coalescence in molded gypsum and carrara marble: Part 1 macroscopic observations and interpretation. *Rock Mech Rock Eng* 42(3):475–511. <https://doi.org/10.1007/s00603-008-0002-4>
- Wong LNY, Einstein HH (2009c) Crack coalescence in molded gypsum and carrara marble: Part 2 microscopic observations and interpretation. *Rock Mech Rock Eng* 42(3):513–545. <https://doi.org/10.1007/s00603-008-0003-3>
- Wong LNY, Li HQ (2013) Numerical study on coalescence of two coplanar pre-existing flaws in rock. *Int J Solids Struct* 50:3685–3706. <https://doi.org/10.1016/j.ijsolstr.2013.07.010>
- Wong RHC, Chau KT, Tang CA, Lin P (2001) Analysis of crack coalescence in rock-like materials containing three flaws—Part I: experimental approach. *Int J Rock Mech Min Sci* 38(7):909–924. [https://doi.org/10.1016/S1365-1609\(01\)00064-8](https://doi.org/10.1016/S1365-1609(01)00064-8)
- Yang L, Jiang YJ, Li SC, Li B (2013) Experimental and numerical research on 3D crack growth in rocklike material subjected to uniaxial tension. *J Geotech Geoenviron* 139(10):1781–1788. [https://doi.org/10.1061/\(ASCE\)GT.1943-5606.0000917](https://doi.org/10.1061/(ASCE)GT.1943-5606.0000917)
- Zhang XP, Wong LNY (2012) Cracking processes in rock-like material containing a single flaw under uniaxial compression: a numerical study based on parallel bonded-particle model approach. *Rock Mech Rock Eng* 45:711–737
- Zhang XP, Wong LNY (2013) Crack initiation, propagation and coalescence in rock-like material containing two flaws: a numerical study based on bonded-particle model approach. *Rock Mech Rock Eng* 46(5):1001–1021
- Zhang XP, Wong LNY (2014) Displacement field analysis for cracking processes in bonded-particle model. *Bull Eng Geol Environ* 73:13–21
- Zhang H, Song HP, Kang YL, Huang GY, Qu CY (2013) Experimental analysis on deformation evolution and crack propagation of rock under cyclic indentation. *Rock Mech Rock Eng* 46(5):1053–1059. <https://doi.org/10.1007/s00603-012-0309-z>
- Zhang XP, Zhang Q, Wu SC (2017) Acoustic emission characteristics of the rock-like material containing a single flaw under different compressive loading rates. *Comput Geotech* 83:83–97
- Zhao C, Matsuda H, Morita C, Shen MR (2011) Study on failure characteristic of rock-like materials with an open-hole under uniaxial compression. *Strain* 47(5):405–413. <https://doi.org/10.1111/j.1475-1305.2009.00701.x>
- Zhao C, Bao C, Matsuda et al (2015) Application of digital image correlation method in experimental research on crack propagation of brittle rock. *China J Geol Eng* 37(5):944–951 (in Chinese)
- Zhao YL, Zhang LY, Wang WJ, Pu CZ, Wan W, Tang JZ (2016) Cracking and stress-strain behavior of rock-like material containing two flaws under uniaxial compression. *Rock Mech Rock Eng* 49(7):2665–2687. <https://doi.org/10.1007/s00603-016-0932-1>
- Zhao C, Ma CC, Zhao CF, Du SG, Bao C (2017) Crack propagation simulation of rock-like specimen using strain criterion. *Eup J Environ Civ Eng*. <https://doi.org/10.1080/19648189.2017.1359677>

Publisher's Note Springer Nature remains neutral with regard to jurisdictional claims in published maps and institutional affiliations.